Comparison of optical and radar measurements of surf and swash zone velocity fields

Jack A. Puleo

Naval Research Laboratory, Marine Geosciences Division, Stennis Space Center, Mississippi, USA

Gordon Farquharson and Stephen J. Frasier

Microwave Remote Sensing Laboratory, University of Massachusetts, Amherst, Massachusetts, USA

K. Todd Holland

Naval Research Laboratory, Marine Geosciences Division, Stennis Space Center, Mississippi, USA

[1]   Surf zone bore celerities and swash zone surface currents were measured on a shallow sloping, low-energy beach using two remote sensing methods that differ fundamentally in their imaging mechanisms. Microwave Doppler radar measures electromagnetic backscatter from small-scale ocean surface roughness while video-based particle image velocimetry (PIV) relies on image texture resulting from variations in light reflectivity from the ocean surface. Imagery from the two methods showed high correlation, in which regions of high radar backscatter corresponded to visibly identifiable waves and bores propagating across the surf zone. Correlation coefficients between radial velocity time series sampled using the two methods at multiple locations across the surf zone were typically greater than 0.5 for frequencies less than a noise cutoff of 0.25 Hz. Similarly, spectra were found to be coherent at the 95% level with a nearly zero phase shift between the two signals near the broad spectral peak between 0.02 and 0.25 Hz. However, some significant differences were evident. PIV was capable of estimating both cross-shore and alongshore surface velocities while the use of one microwave Doppler radar system restricted surface velocity estimates from that technique to line of sight (radial) only. PIV was found to be more capable of estimating swash zone (uprush and backwash) surface velocities as a smoother water surface in the swash zone adversely affected radar reflectivity. In contrast, microwave Doppler radar was found to be more capable of estimating the surface velocity between bores when insufficient image texture was recorded in the video imagery. Both techniques were capable of measuring surf zone bore celerities through comparison to a shallow water model and to independent celerity estimates extracted from the slope of individual bore trajectories. Typical normalized errors were roughly 25% for radar and 15% for PIV.   *INDEX TERMS:* 4275 Oceanography: General: Remote sensing and electromagnetic processes (0689); 4546 Oceanography: Physical: Nearshore processes; 3020 Marine Geology and Geophysics: Littoral processes; *KEYWORDS:* particle image velocimetry, Doppler radar, remote sensing, nearshore currents

1.   Introduction

[2]   The coastal ocean is a dynamic region where breaking waves and currents mobilize and transport sediments reshaping the underlying bathymetry and coastal morphology. These sediment processes in turn influence the wave and current patterns inducing a feedback mechanism. An understanding and predictive capability of these processes is necessary for engineering practices in coastal land use policy and erosion mitigation. Typical field studies involve the emplacement of several current meters or wave gauges. While it is known that nearshore fluid motions and wave fields are typically nonuniform in the alongshore direction (i.e., three dimensional), cost and deployment logistics tend to force sparse cross-shore arrays. In order to increase the sampling region, remote sensing methods that are cost effective and can sample large spatial regions are required. Two such methods include radar and video-based imaging.

[3]   The use of video methods for nearshore processes research has gained increasing interest and acceptance in the

scientific community [*Holman et al.*, 1993; *Holland et al.*, 1997]. The thrust of video-based research has focused on describing the nearshore morphology such as sandbar migration [*Lippmann and Holman*, 1989, 1990], beach configuration [*Holman et al.*, 1991; *Holland and Holman*, 1997], bathymetry estimation [*Stockdon and Holman*, 2000; *Dugan et al.*, 2001b] and wave information such as phase speed, period and direction [*Lippmann and Holman*, 1991; *Dugan et al.*, 1996, 2001a]. Video data have also been used to estimate the mean alongshore current in the nearshore [*Chickadel and Holman*, 2001]. Comparisons with near-bottom-mounted current meters have shown high correlations, but these were restricted to mean flows rather than instantaneous motions. Video-based methods have also included the use of particle image velocimetry (PIV) which has been used to investigate the vertical flow structure under breaking and nonbreaking waves [*Gray and Greated*, 1988; *She et al.*, 1997; *Chang and Liu*, 1998] and the fluid motion over a rippled bed [*Earnshaw et al.*, 1994]. More recently, PIV has been used to extract instantaneous surface current velocities in the swash zone of a high energy beach [*Puleo and Holland*, 2000; *Holland et al.*, 2001].

[4] Similarly, microwave radar has been used extensively in remote sensing of the ocean surface. Airborne along-track interferometric synthetic aperture radar (InSAR) has been used to measure energy density spectra and to derive current estimates for the ocean surface in the nearshore region [*Marom et al.*, 1991; *Shemer et al.*, 1993] and for current estimation in deeper water [*Graber et al.*, 1996]. From land-based radars, time series of radar intensity images have been used to produce frequency-wave number spectra using standard marine navigation radars [*Young et al.*, 1985; *Wolf and Bell*, 2001] and attempts have been made to estimate surface currents from the sequences by measuring the deformation of the frequency-wave number dispersion relationship [*Frasier and McIntosh*, 1996; *Senet et al.*, 2001]. However, in the surf and swash zones where the waves refract and shoal over varying bathymetry, these traditional techniques are suspect as they rely on a statistically homogeneous wave field. Other methods involving image analysis have also been used to obtain wave direction and celerity from marine navigation intensity images [*Bell*, 1999]. However, standard marine navigation radars use horizontally polarized electromagnetic radiation to minimize sea clutter, which, for wave studies, is the desired signal. Horizontally polarized backscattered energy is also highly nonlinear at low grazing angles, making it difficult to directly relate intensity to the wave spectrum. In contrast, direct measurement of the Doppler shift due to line of sight velocities with a vertically polarized microwave Doppler radar provides a more direct method of estimating surface currents and directional wave spectrum [*Frasier et al.*, 1995; *Poulter et al.*, 1995; *Frasier and McIntosh*, 1996; *McGregor et al.*, 1997]. This technique has also been used to measure the relationship between surface currents and subsurface current structure [*Moller et al.*, 1998] and to estimate bathymetry and wave energy fluxes and dissipation across an offshore bar [*McGregor et al.*, 1998] in water depths of several meters. Microwave Doppler radar techniques have occasionally been used inside the surf zone [*Ruessink et al.*, 2002], but only in relation to sandbar crest position.

[5] The measurements presented in this paper were used to compare and interpret both PIV and microwave Doppler radar measurements of nearshore currents and waves. In this paper, we present observations of the nearshore region incorporating the surf and swash zones using both techniques. Section 2 describes the field experiment, site layout and the principles of video and radar imaging. Section 3 details the methods used for extracting velocities from imagery. Velocity measurements, results and validation are given in section 4. Discussion and conclusions are presented in sections 5 and 6.

2. Field Experiment

2.1. Site Layout

[6] A nearshore field experiment was conducted at Scripps Beach in La Jolla, California, from October 2 to October 10, 2000. The beach is situated south of the Scripps Canyon and north of the pier at the Scripps Institute of Oceanography. Scripps Beach is a shallow sloping (gradient ~1/50) fine sand beach. Semidiurnal tidal range is about 1.5 m and wave heights are typically much smaller than 1 m. During the experiment, radar and video measurements overlapped for several 20-min data segments between October 8 and October 10. A representative 20-min segment of data collected on October 10, when wave heights and wind speeds were sufficient for both techniques to be utilized, is presented. Specifically, the significant wave height (measured at the pier end) was roughly 1 m with a peak period of about 5 s (wave heights for the previous days were typically less than 0.5 m). The wind speed averaged 4.5 m s^{-1} and was roughly onshore from 283° true north.

[7] Two analog video cameras were fixed atop the Center for Coastal Studies (CCS) building overlooking the area of interest with a total coverage of about 100 m in the alongshore and 250 m in the cross shore. The pixel footprint in the near field was roughly 0.1 × 0.1 m. The radar system was located on the roof just south of the camera location. The radar field of view (which significantly overlapped that of the cameras) covered a 30° azimuthal sector with a resolution of 0.5° and 384 m in range with a resolution of 3 m. Figure 1 shows the position of the footprints for each of the sensors. The alongshore coordinate increases to the north and the cross-shore coordinate in the offshore direction. Beach and offshore bathymetry surveys were obtained with a kinematic GPS system onboard a subaerial profiling pushcart or jet ski water craft.

2.2. Radar and Video Imagery

[8] Figure 2a shows a relative backscattered power image collected from the radar system. The bright areas correspond to regions of high backscatter and the darker regions to areas of low backscatter. The dashed line is the radar centerline for which range-time comparisons will later be made. A corresponding geo-rectified camera snapshot image is shown in Figure 2b, where, for clarity, the portion of the image outside the radar field of view has been removed. Here, the dark regions correspond to areas with little wave breaking whereas the brighter regions, especially between x = 100 to x = 120 m, correspond to the wave breaking and foam generation. The regions of breaking and high backscatter show a strong visual corre-
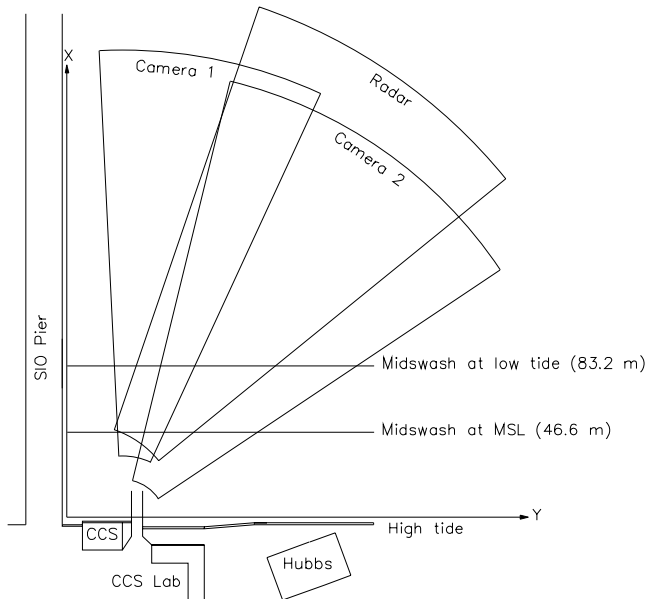
Figure 1. Schematic of Scripps Beach showing the imaging footprints for the two analog cameras and the radar system. The radar was positioned on top of the left-hand corner of the CCS building and the cameras were on the top right-hand corner.

lation giving confidence that the two methods are sampling similar features. Radar is also capable of observing unbroken waves as shown by the high backscatter intensity observed in the radar image near $x = 140$ m. Unbroken waves are not as readily discernible in the geo-rectified video image as only a weak increase in image intensity is observed near $x = 140$ m.

[9] In Figure 3, two oblique video images separated by roughly 2 s are shown. The colored lines are the contours of

backscattered radar power at 90 (blue) and 100 (red) dB. In both images, high backscattered power is recorded where the shoreward propagating bores are located as evidenced by the red contours overlaying the landward edges of the bright regions in the image. In the image at 17:32:54.66, a wave is seen offshore that has an unbroken section. The backscattered power is higher at the broken sections and is less in the unbroken section where the wave is steepening. In the second image at 17:32:56.62, where most of the wave has broken, the high power contours extend through a larger region of breaking and the 90-dB contour is more continuous across the wave front. Offshore of this wave there are still areas of high backscatter, but because of the obliquity of the image, individual waves are difficult to see in the video view at this distance. These images suggest that the radar system measures wave steepening and wave breaking that is simultaneously observed by the video system.

[10] Further qualitative comparison between the two methods can be obtained using a range-time image (Figure 4). A range-time image is created by plotting the backscattered (or image) intensity along a single transect (the radial centerline in Figure 2) over time and is useful for tracking wave crest propagation across the surf zone. Further, since the data are in time-distance space, the slope of the features represents a component of the bore phase velocity which will be larger than the shoreward directed phase velocity of the bore. Individual waves can be seen as the brighter curved features. The patterns have curvature because the wave celerity decreases with decreasing water depth. The shading bar represents the radar relative backscattered power (dB) or the dimensionless image intensity.

[11] Although the patterns observed with the two methods are similar, individual waves are more readily visible in the radar range-time image because the backscatter is related to the bore elevation and slope of the water surface whereas for the video range-time image, the relation between pixel intensity and bore location depends on lighting angles and
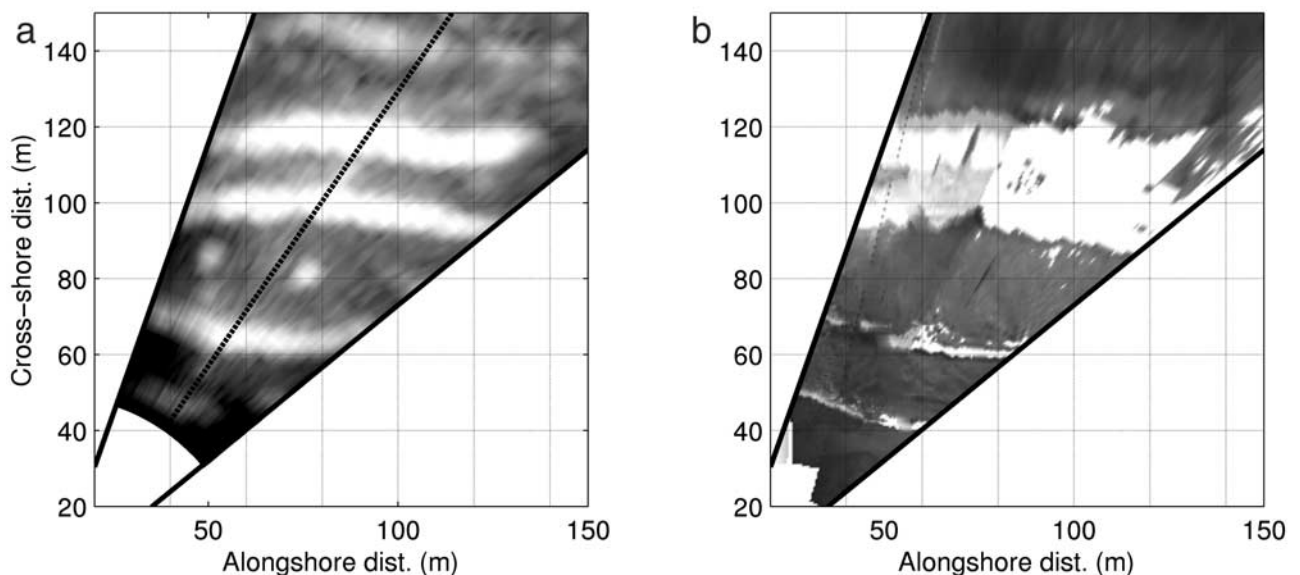

Figure 2. (a) Radar snapshot of the backscattered power and the radial centerline (dashed line). Solid lines demarcate radar field of view. (b) Merged video snapshot from both analog cameras excluding the portion outside radar field of view.
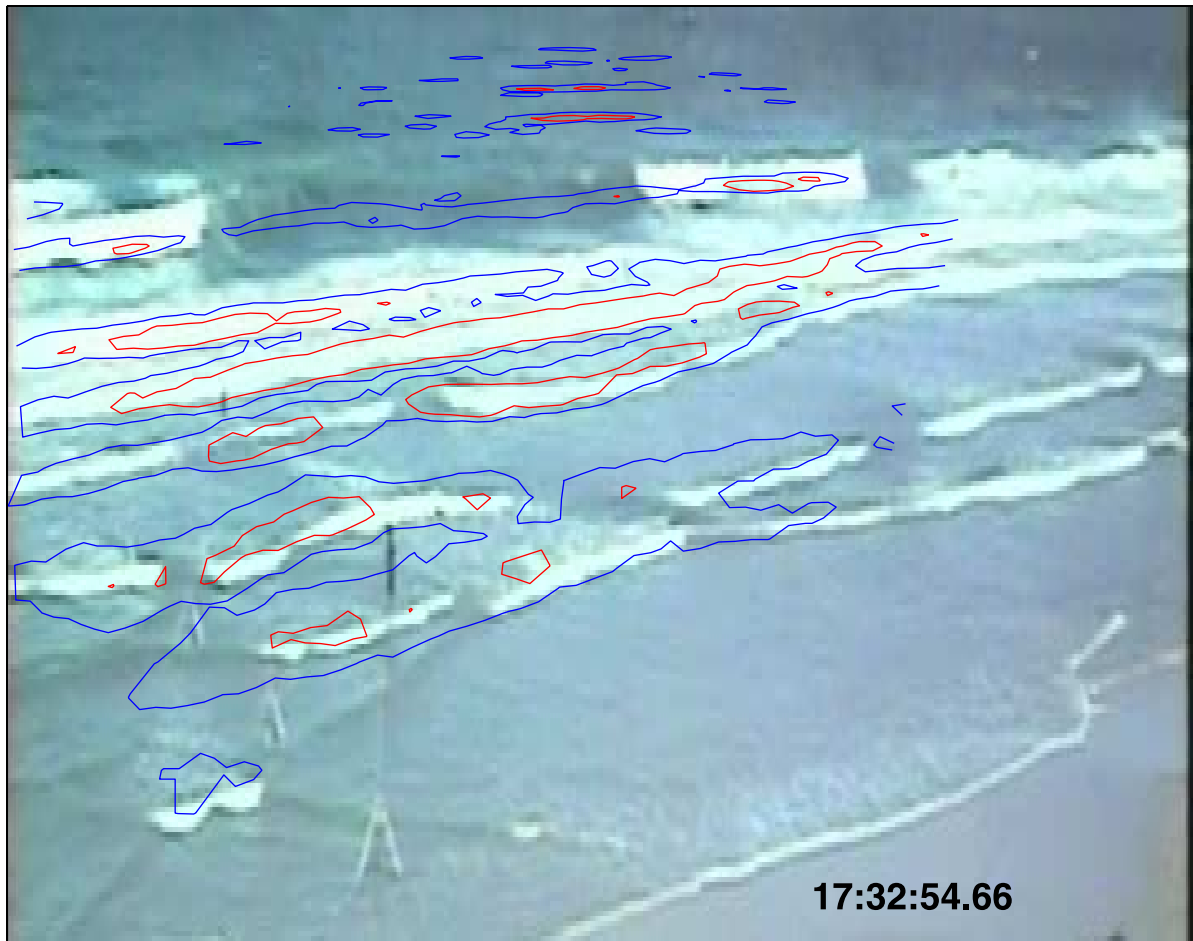
Figure 3. Oblique video images with backscattered radar power contour levels of 90 (blue) and 100 (red) dB superimposed. Wave height was not taken into account when overlaying the contour levels, causing some of the misregistration. Image times are shown as hours:minutes:seconds in GMT.

contrast changes in remnant surface foam, which causes the wave features to appear less distinct. However, both techniques clearly record the same wave fronts and are able to capture wave interactions. An example of these wave interactions can be seen just prior to $t = 17h32$ (GMT) where two features merge due to a second wave front overtaking the preceding one. The breaking region is also captured in both images as evidenced by the rapid change in intensity indicating wave breaking at a radial distance of approximately 175 m. The physical reason for a change in the video signal is obvious because the sea surface intensity actually changes from dark to light due to foam and bubble generation. The change in backscattered radar intensity is an increase in surface roughness to scales comparable to or larger than the electromagnetic wavelength. Although neither technique estimates wave amplitude directly, the comparisons between radar and video imagery suggest that these remote sensing techniques image similar surface features, such as wave crests, in the nearshore region.

3. Methods of Velocity Extraction

3.1. Radar

[12] The radar used in this study is the Focused Phased Array Imaging Radar (FOPAIR) [*McIntosh et al.*, 1995], a dual-polarized X-band (10 GHz) Doppler radar designed to image the sea surface with meter scale spatial resolution. The radar uses a linear receive array and digital beamforming techniques to obtain azimuth resolution of 0.5°, and pulse compression to achieve range resolution of 3 m. The radar is capable of both vertical and horizontal polarization measurements. However, only vertically polarized measurements are considered in this study.

[13] At incidence angles sufficiently removed from nadir, the microwave (>1 GHz) reflectivity of the ocean waves with small surface slopes compared to the electromagnetic wavelength, is dominated by resonant interaction between the incident electromagnetic waves and small capillary and capillary-gravity waves (Bragg scattering) [*Wright*, 1968]. Contrast in microwave radar images is obtained through the modulation of this mean reflectivity through tilting of the local incidence angle (tilt modulation) and straining and compressing of the shorter waves (hydrodynamic modulation). Surface fluid velocities are measured from the line of sight Doppler shift due to the wave velocity. In the Bragg scattering model the velocity measured by the radar is comprised of the phase velocity of the resonant capillary waves superimposed on any surface current that might be present. When the spatial resolution of the radar is sufficient to resolve long wave features such as gravity waves, the

Figure 3.   (continued)

velocity measurement also includes the radial component of the instantaneous orbital velocity of the longer waves in addition to the capillary wave velocity.

[14] The Doppler shift in the received electromagnetic wave is estimated by the FOPAIR system through a covariance or "pulse pair" technique applied to successive radar images. The pulse pair calculation is an estimation of the first moment of the Doppler spectrum [*Miller and Rochwarger*, 1972]. The radar forms an image of the ocean surface over a period of approximately 0.64 ms, which is well within the decorrelation time for microwave backscatter at X-band [*Plant et al.*, 1994]. A second image is captured about $\tau = 1.5$ ms later and the covariance $C(t, \tau)$ of the images is formed. The covariances for several image pairs are averaged over a period of 0.5 s to obtain Doppler radar velocity estimates using

$$v(t) = \frac{\lambda}{2\pi} \frac{\phi(t)}{2\tau \sin\theta_i}, \tag{1}$$

where λ is the wavelength of the transmitted electromagnetic wave, θ_i is the angle of incidence from the antenna to the ocean surface. The argument of the covariance function, $\phi(t)$, is the phase difference of the radar return between successive radar pulses and is proportional to the change in distance that the scattering feature has moved over the time period τ.

3.2. Particle Image Velocimetry

[15] In a similar way to radar, PIV uses correlation of image pairs to measure wave propagation. However, rather than electromagnetic backscatter, the image intensity represents a combination of brightness changes due to wave breaking and changes resulting from light reflection off the slope of the water surface relative to the sun angle as viewed from the camera. The assumption is that the motion of the image texture (tracer) created by spatial variations in the image intensity travels at the flow velocity. Somewhat analogous to the radar system's dependence on a sloped surface (capillary or gravity waves), difficulties for PIV result when insufficient texture is recorded by the imagery.

[16] The PIV technique used is fully described by *Holland et al.* [2001], and only a brief description will be given here. Two images separated in time by Δt are digitized from time sequence imagery and geo-rectified to a common ground plane [*Holland et al.*, 1997]. A small interrogation window, I, is selected about the grid point in the first image and compared to many search windows, S, of the same size in the second image. Comparisons are made using an error correlation function, Φ, [*Hart*, 1998],

$$\Phi_{\Delta x, \Delta y} = 1 - \frac{\sum\limits_{1}^{a} \sum\limits_{1}^{b} (|I - S|)}{\sum\limits_{1}^{a} \sum\limits_{1}^{b} (I + S)}, \tag{2}$$
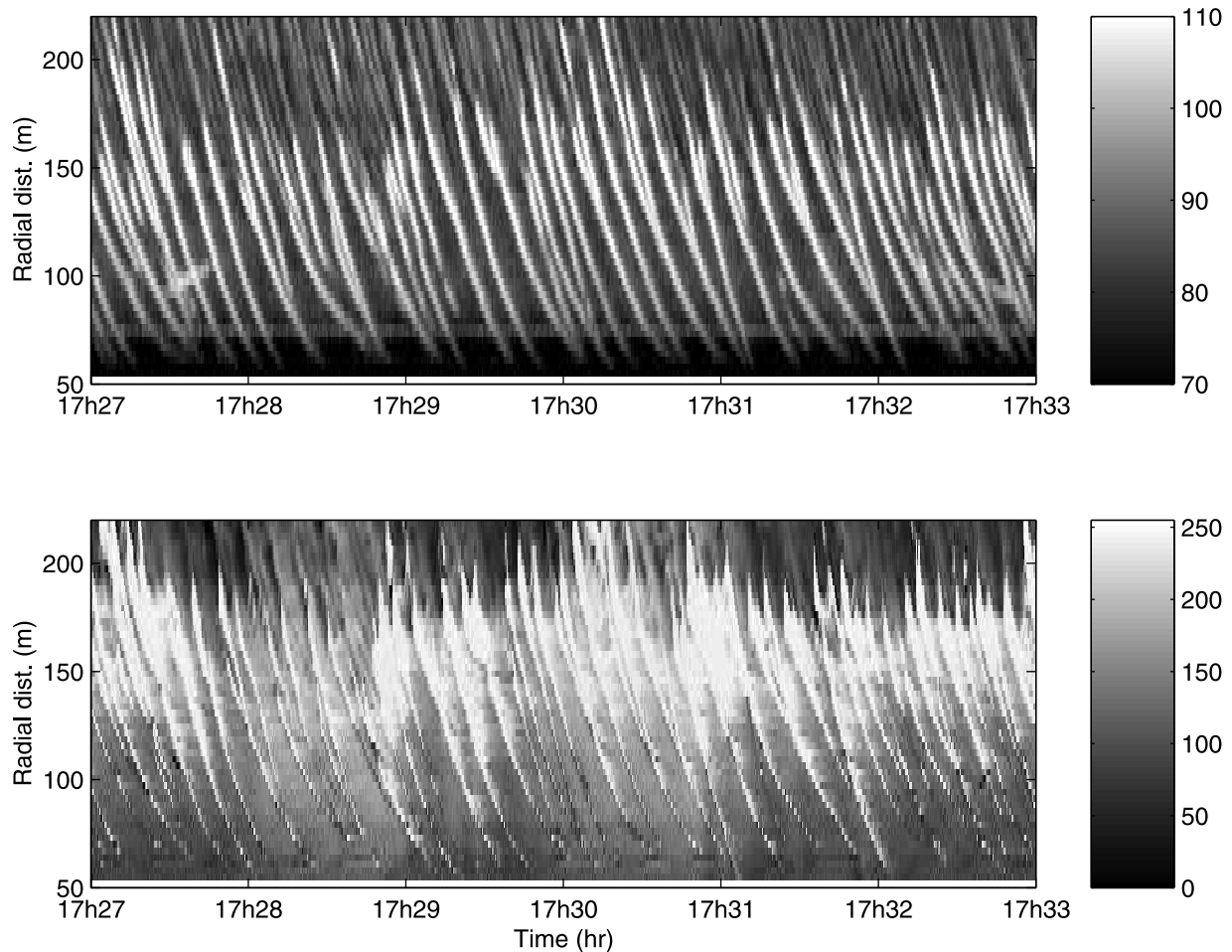
Figure 4. Range-time images for (top) radar and (bottom) PIV generated along the radial centerline of the radar footprint. The shading bar represents the relative backscattered power (dB) for the radar and the scaled image intensity for the video image.

where a and b are the dimensions of I and Δx and Δy are the spatial offsets.

[17] The peak in the correlation matrix is fitted with a 2D Gaussian shape to yield the horizontal offsets to subpixel accuracy. When these offsets are divided by the image separation time, 2D surface velocity vectors are obtained. As with most PIV approaches, post-processing is applied to the velocity field to remove spurious vectors (see *Holland et al.* [2001] for details).

4. Results

4.1. Radar-PIV Comparisons

[18] PIV and radar velocities were collected between 17:19 and 17:39 (GMT) from several locations across the surf zone at cross-shore positions $x = 50, 60, 70, 75, 80, 90,$ and 100 m from the shoreline. The PIV data was collected at 2.5 Hz and the radar data at roughly 2 Hz. The radar Doppler velocities were subsequently linearly interpolated to the same 2.5 Hz sampling times as the PIV data. The velocity component in the direction of the radar line of sight was computed from the PIV velocity vectors through a coordinate system rotation. As a consequence of the coordinate system, negative velocities are directed toward the radar

system and positive velocities away from the radar system. Six minutes of the time series are shown in Figure 5. The shaded lines are radar and the black lines are PIV with each successive pair of time series offset by 5 m s^{-1}. The time series show the maximum radial velocities increasing in the offshore direction and ranging from about -2.5 to -5 m s^{-1}. In both cases, the velocities generally do not become positive, thus indicating movement away from the sensor is infrequently measured. At all cross-shore locations except at $x = 50$ and $x = 100$ m the time series are well correlated (Table 1) and indicate that peak radar and PIV velocities are nearly equal. The highest correlations (all are significant at the 95% level) are observed between $x = 60$ and $x = 90$ m with a decrease in correlation for the swash zone and offshore positions. When high-frequency noise (>0.25 Hz) was excluded from the calculation of the correlation coefficient, the r^2 values increased slightly (Table 1).

[19] Mean PIV velocities calculated from the seven locations, however, show that mean radar velocity magnitudes are consistently larger than PIV velocity magnitudes (Table 2). Mean PIV velocities range from -0.55 to -0.79 m s^{-1} but tend to cluster near -0.75 m s^{-1} (except $x = 50$ m and $x = 100$ m) while mean radar velocity magnitudes
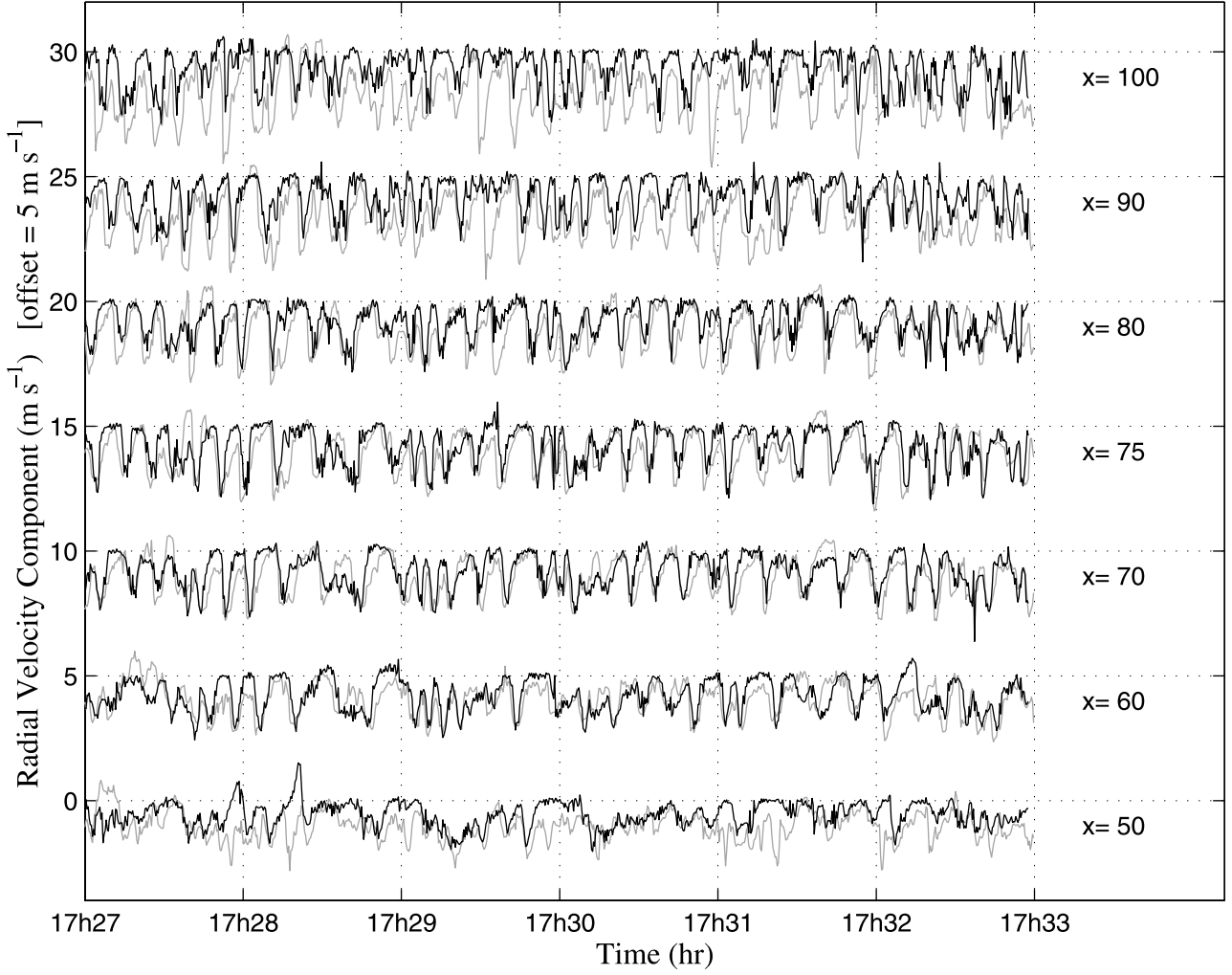
Figure 5. Radial velocity time series comparison between radar (shaded lines) and PIV (black lines) at seven cross-shore locations. Successive time series are vertically offset by 5 m s^{-1}.

range between -1.07 to -1.94 m s^{-1}. In all cases, PIV standard deviations are roughly equal to the mean PIV velocities indicating the scatter in the data is as large as the velocity estimate whereas radar velocity standard deviations show an increase with offshore distance and are larger than PIV standard deviations.

[20] A measure of the difference between the time series can be determined by

$$E_{\alpha,\beta} = \frac{\langle \beta - \alpha \rangle}{|\langle \beta \rangle|} \pm \frac{\sigma_{\beta-\alpha}}{|\langle \beta \rangle|}, \qquad (3)$$

where α, β are the time series of interest, here PIV and radar, respectively, σ is the standard deviation, angle brackets denote averaging and $| \ |$ denote magnitude. $E_{\alpha,\beta}$ is a measure of the normalized mean difference and the spread about that mean given by the normalized standard deviation. In a similar way to mean radar Doppler and mean PIV velocities, $E_{PIV,Doppler}$ (Table 2) tends to increase in the offshore direction and the scatter is nearly as large as the mean difference itself. Note that $E_{\alpha,\beta}$ can be thought of as a normalized relative error if it is assumed that the variable β represents the true value (see validation section).

Table 1. PIV/Radar Time Series Correlation

Cross-Shore Location	r^2 Correlation Coefficient	r^2 Correlation Coefficient (After Filtering)
x = 50	0.15	0.18
x = 60	0.38	0.43
x = 70	0.48	0.56
x = 75	0.43	0.52
x = 80	0.48	0.59
x = 90	0.46	0.60
x = 100	0.27	0.37

Table 2. PIV/Radar Time Series Statistics

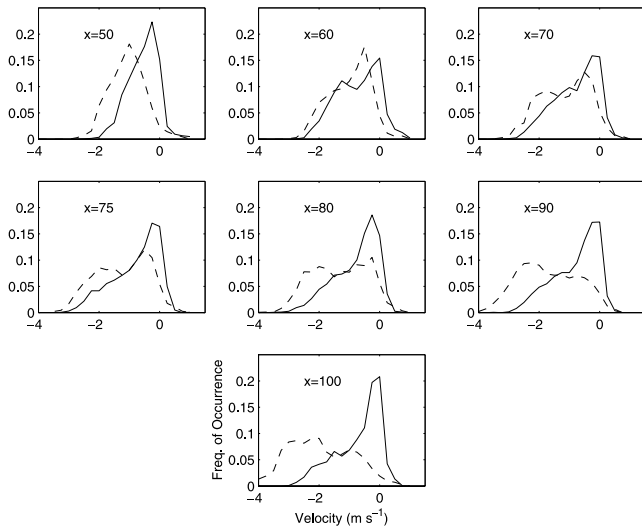| Cross-Shore Location (Radial Distance From Radar), m	PIV mean ± 1 std, m s^{-1}	Doppler radar mean ± 1 std, m s^{-1}	$E_{PIV,Doppler}$
x = 50 (82.9)	-0.55 ± 0.51	-1.07 ± 0.58	-0.49 ± 0.56
x = 60 (89.0)	-0.73 ± 0.70	-1.00 ± 0.68	-0.27 ± 0.61
x = 70 (95.7)	-0.78 ± 0.72	-1.14 ± 0.81	-0.33 ± 0.53
x = 75 (99.2)	-0.79 ± 0.77	-1.23 ± 0.87	-0.36 ± 0.56
x = 80 (102.9)	-0.78 ± 0.72	-1.31 ± 0.91	-0.41 ± 0.51
x = 90 (110.6)	-0.79 ± 0.74	-1.69 ± 0.98	-0.54 ± 0.43
x = 100 (124.6)	-0.70 ± 0.75	-1.94 ± 1.04	-0.65 ± 0.47

Figure 6. PIV (solid line) and radar (dashed line) velocity histograms for the seven cross-shore locations. Axis labels for lower panel apply to all panels.
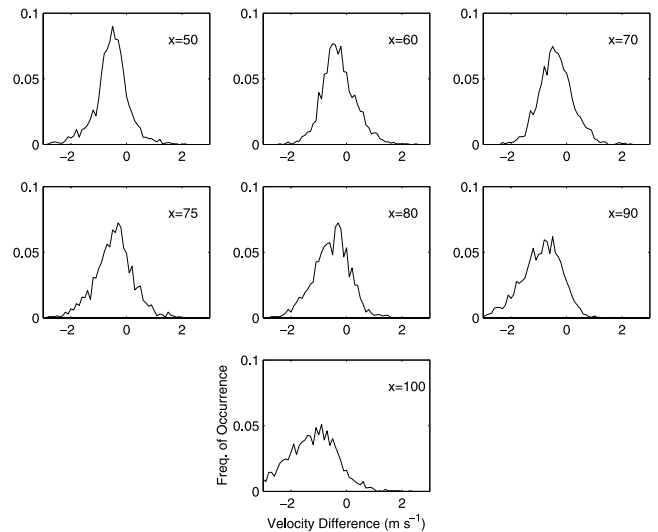

Figure 7. Histograms of velocity differences between radar and PIV for the seven cross-shore locations. Axis labels for lower panel apply to all panels.

[21] Histograms were computed to show similarities and differences in the distribution of surface velocities from the PIV and radar techniques (Figure 6). The histograms indicate that both radar and PIV sampled predominantly onshore (negative) velocities with magnitudes increasing with offshore location and showing some variability across the surf zone. At $x = 50$ m (swash zone) the velocity histograms are shifted with the radar displaying a Gaussian-type shape. From $x = 60$ to $x = 80$ m (inner surf zone), the histograms have more similar shapes although PIV tends to be more negatively skewed than the radar and a bimodal structure in the radar histograms becomes apparent. The radar peak near -2 m s^{-1} increases with offshore distance while the peak near zero velocity decreases. In contrast, the PIV peak near zero velocities increases in the offshore direction causing the difference between the peaks of the histograms to increase as well. At $x = 90$ and $x = 100$ m (shoaling or breaking region) the radar does not show a clear peak near zero velocity and instead has a broad peak near -2.25 m s^{-1}. However, PIV still shows a strong peak near zero velocity.

[22] Velocity difference histograms (Figure 7) show that the radar velocity magnitudes are generally larger than those measured by PIV. They also display a trend of increasing difference in the offshore direction (with the exception of the swash zone [$x = 50$ m]). Hence, radar and PIV velocities are most similar in inner surf zone and differ more throughout the mid surf zone to the breaking region (Table 2). Standard deviations of the differences range between 0.60 and 0.73 m s^{-1} except at $x = 100$ m, where the value is 0.91 m s^{-1}.

[23] In a spectral sense, the velocity signals are also similar. Example energy spectra for $x = 70$ m are shown in Figure 8a for PIV (solid line) and radar (dashed line). Spectra were calculated using a Kaiser-Bessel window on each of 512 ensembles with 50% overlap and band averaged over two adjacent frequency bands. Both plots show a broad spectral peak near 0.071 s^{-1} ($\sim$14 s), which is more than double the incident peak period measured at

the pier end. Spectral estimates are similar until about $f = 0.7$ s^{-1} when the curves diverge. The squared coherence is shown in Figure 8b along with the 95% confidence level (dotted). Over 80% of the spectral energy is contained under the spectral peak from $f = 0.02$ to 0.25 s^{-1}. The squared coherence is significant at the 95% confidence level in this frequency range with values approaching 0.85 and rapidly decays above incident wave frequencies of 0.25 s^{-1}. Phase estimates with 95% confidence limits span zero phase throughout the region of high coherence (Figure 8c). Note that phases are only shown when the coherence exceeds the 95% confidence limit. This analysis indicates that the time series are nearly in phase in low
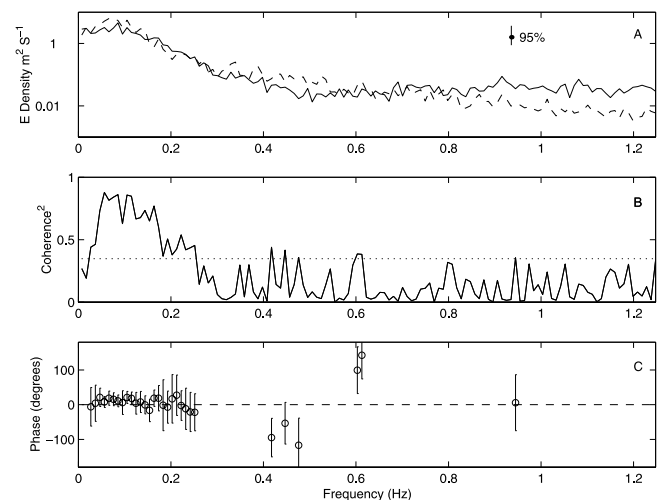

Figure 8. (a) Auto-spectra of time series collected at x = 70 and y = 60 for radar (dashed line) and PIV (solid line). The 95% confidence bar is also shown. (b) Squared coherence values (solid line) and 95% confidence level (dotted line). (c) Phase between the time series with 95% confidence bars. Note that phases are only shown for significant coherence squared.

Table 3. Bore Celerity Statistics for Radial Range-Time, PIV and Doppler Bore Celerities

Cross-Shore Location (Radial Distance From Radar), m	Range-Time Mean ± 1 std, m s^{-1}	PIV Mean ± 1 std, m s^{-1}	Doppler Mean ± 1 std, m s^{-1}	$E_{PIV,range-time}$	$E_{Doppler,range-time}$
x = 50 (82.9)	−1.37 ± 0.36	−1.39 ± 0.45	−1.97 ± 0.47	0.01 ± 0.36	0.43 ± 0.33
x = 60 (89.0)	−1.65 ± 0.31	−2.08 ± 0.39	−2.08 ± 0.49	0.26 ± 0.28	0.26 ± 0.32
x = 70 (95.7)	−1.88 ± 0.31	−2.14 ± 0.32	−2.35 ± 0.43	0.14 ± 0.19	0.25 ± 0.24
x = 75 (99.2)	−1.98 ± 0.32	−2.31 ± 0.35	−2.50 ± 0.39	0.17 ± 0.20	0.27 ± 0.22
x = 80 (102.9)	−2.08 ± 0.33	−2.16 ± 0.40	−2.72 ± 0.40	0.04 ± 0.23	0.31 ± 0.22
x = 90 (110.6)	−2.26 ± 0.35	−2.16 ± 0.47	−3.00 ± 0.45	−0.04 ± 0.25	0.33 ± 0.17
x = 100 (124.6)	−2.42 ± 0.39	−1.98 ± 0.41	−3.31 ± 0.49	−0.18 ± 0.27	0.37 ± 0.22

frequency to incident band. Spectra for the other cross-shore locations are similar to the one shown here except at $x = 50$ and $x = 100$ m. At $x = 50$ m the broad spectral peak occurs near $f = 0.03$ s^{-1} (not shown). A broad region of coherence is not observed at this location with the squared coherence being significant at just several frequencies, reiterating the dissimilarity between the time series in the swash zone. At $x = 100$ m, the spectral peak is near $f = 0.085$ s^{-1} and the region of high squared coherence is narrower extending from $f = 0.03$ to 0.12 s^{-1} (not shown).

4.2. Validation

[24] The range-time image (Figure 4) can be used to estimate the radial component of the bore propagation velocities in the surf zone and can be compared with corresponding velocities measured by the radar Doppler and PIV. Although the range-time images are created from data collected by the same remote sensing systems, the manner in which velocities are extracted (slope of trajectory) is different from either the PIV or "pulse pair" radar technique and serves as an independent bore celerity estimate. However, since the range-time data yields only bore celerity information, these data cannot be used to validate the surface velocities between bores.

[25] For comparison, 39 representative bore trajectories determined from the bright curves in the radar range-time data were selected where the bore signature was clearly visible from a radial distance of 75 to 125 m and where shoreward propagating bores did not capture and overtake one another (e.g., where bright curves in Figure 4 do not coalesce). The bore trajectories were then fit with a second-order polynomial, and the radial bore velocity was calculated for each radial distance corresponding to the seven cross-shore locations by taking the derivative of the polynomial, evaluating at each location and accounting for the oblique direction of the radial centerline over which the radar range time-image was created (Table 3). The mean range-time derived bore celerities obtained from the polynomial fits decrease (in magnitude) in the landward direction from about −2.4 m s^{-1} to −1.4 m s^{-1} (Table 3). PIV and Doppler velocities corresponding to the range-time derived bore celerities at the same cross-shore distance are also given in Table 3 (these values differ from those in Table 2 since only PIV and Doppler velocities corresponding to the range-time derived bore celerities, rather than the whole time series, are used). In a similar way to the mean range-time bore celerities, the corresponding Doppler velocities tend to decrease (in magnitude) in the landward direction as does PIV except at the offshore location. However, the normalized mean relative error between

range-time bore celerities and PIV varied between 1 and 26% whereas the normalized mean relative error between range-time bore celerities and Doppler varied between 25 and 43%.

[26] PIV and Doppler bore celerities can be further validated by comparison to a shallow water wave dispersion relationship. Dispersion relationships have been previously used to infer the water depth using measurements of wave celerity [e.g., *Holland*, 2001]. In this case, however, we estimate bore celerities from measured water depths. The shallow water dispersion relationship used here accounts for finite amplitude effects and has the form

$$c = \sqrt{g(h + H)} = \sqrt{1 + \gamma}\sqrt{gh}, \quad (4)$$

where c is the theoretical bore celerity, h is the water depth (obtained from bathymetry surveys), H is the wave height, γ is a coefficient relating wave height to water depth and g is gravitational acceleration. The constant γ was set to a value of 0.5, roughly the value found by *Raubenheimer et al.* [1996] for this beach and similar wave conditions (although choice of other appropriate values for γ has little effect on overall trends). For comparison (Figure 9), radial Doppler and PIV bore celerities were geometrically transformed to lie along the radial centerline. The radial component of the
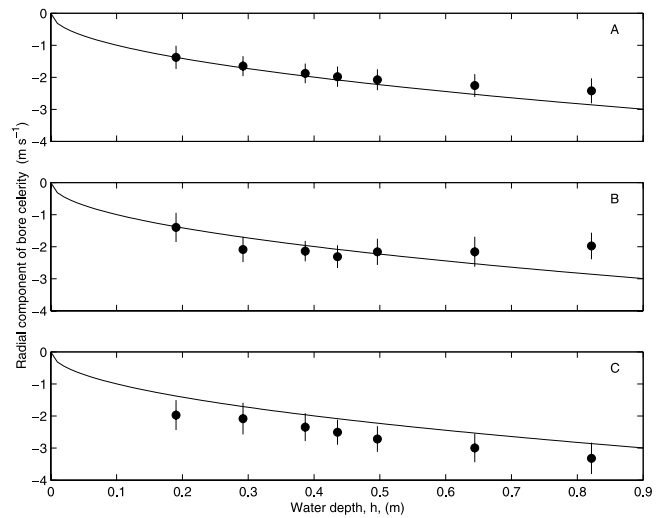

Figure 9. (a) Radial range-time, (b) PIV, and (c) radar bore celerity comparisons to radial component of shallow water dispersion relationship. Dots are mean bore celerities and error bars are 1 standard deviation. The curved line is the bore celerity predicted by equation (4).

theoretical bore celerity was obtained by assuming shore normal waves. Note again that celerities are negative due to the coordinate system used in this study. Results indicate that the radar range-time bore celerity estimates (solid dots with 1 standard deviation error bar) closely match those of the shallow water model (solid line) corroborating our use of these estimates as one form of validation (Figure 9a). PIV estimates of bore celerities closely match the shallow water dispersion relationship (Figure 9b) with normalized relative errors of about 15% excluding the location at $x = 100$ m. Conversely, Doppler estimates of bore celerities follow the trend of the shallow water model but tend to over predict at all depths (Figure 9c) with normalized relative errors of about 25% excluding the location at $x = 50$ m.

5. Discussion

[27] The previous sections have shown PIV and Doppler radar measurements made across the surf and swash zones and comparisons to estimated bore celerities from range-time images and a shallow water model. Although the two techniques often obtained similar velocity estimates, noticeable differences occurred and can generally be related to various subregions of the nearshore as described below.

[28] Offshore ($x = 90$ and $x = 100$ m), the lack of significant image texture (frequently unbroken waves) and decreased pixel resolution may yield erroneous results from the PIV. For example, just prior to 17h31 at $x = 90$ and $x = 100$ in Figure 5, a velocity signal observed in the radar data does not appear in the PIV data. However, using the velocity signature as a wave tracer and invoking a principle of continuity in time and space it is clear from both sensor time series that the wave observed from $x = 80$ to $x = 60$ must have also existed at $x = 90$ and $x = 100$. This lack of texture was the likely cause of a large number of near zero velocities in the PIV histograms at all locations (Figure 6).

[29] Within the surf zone, the onset of breaking and bore propagation changes the nature of the radar backscatter to include more specular or non-Bragg scattering and provides sufficient image texture for PIV such that the instruments measure velocities more indicative of the bore celerity. Also, the change in pixel footprint between the radar and PIV leads to different spatial averaging which may contribute to the differences in the derived velocities. From the inner surf zone to the breaking region, the histogram shapes become less similar as PIV develops a larger peak near zero velocity whereas radar has a bimodal structure. Changes in the PIV histogram with offshore location result from a decrease in surface texture due to the decrease in broken wave propagation. The decrease or lack of surface texture, and hence a tracer, causes the PIV method to return zero or near zero velocity except when a wave crest is within the interrogation window. The bimodal shape of the radar histograms changes across the surf zone as well. However, from the inner surf zone to the breaking region, the peaks shift with the larger velocity peak becoming more dominant implying two competing scattering mechanisms that vary across the surf zone.

[30] In the swash zone, away from shoreward propagating bores, the radar signal-to-noise ratio decreased by 10 dB. As radar relies on surface roughness, the water surface may be too smooth to yield a sufficient radar echo to obtain a reliable velocity estimate from the radar causing a large difference between the radar and PIV velocities. In this zone, the histograms consisted of only one peak and the shapes were similar, but because the PIV velocities were typically smaller, the histograms are offset from each other.

[31] To further investigate the bimodal nature of the histograms, the mean values of each modal distribution were estimated. The mean values of the more negative modal distribution decrease (in magnitude) steadily from offshore to onshore from roughly -2.6 to -1.5 m s^{-1}, indicative of the decrease in wave celerity with decreasing depth. This is also consistent with the curved shapes of the shoreward propagating bores (and velocities derived from them; Table 3) in the range-time images. Thus, it is likely that the significant mechanism contributing to velocities in this modal distribution is attributed to the phase speed of the bore fronts.

[32] The mean of the less negative (slower) peak in the PIV histograms is constant at around -0.2 m s^{-1}. This can be attributed to the large number of near zero velocities due to a lack of sufficient surface texture as discussed previously. In contrast, the mean values for the slower peak in the radar histograms are roughly constant around -0.5 m s^{-1} for $x = 60$ to $x = 75$ m and increase from -0.5 m s^{-1} to roughly -0.9 m s^{-1} for $x = 80$ to $x = 100$ m. These velocities are significantly less than the bore speeds and probably indicative of measurements of the water surface between bores. In this region, the surface would not have a dominant scattering feature (e.g., a bore) and these velocities would be attributed to a distributed scattering mechanism such as Bragg scattering. In deep water conditions, Doppler velocities are a combination of a surface drift, the phase velocity of the Bragg resonant waves, and any surface current present. However, in the surf and swash zone environments, interpretation of these velocities is more complex. One might expect the largely mechanically generated capillary wave spectrum between bores to be directionally broad and mostly isotropic. This would imply little or no bias due to the Bragg resonant capillary wave velocities. However, the effect of onshore-directed wind on these waves might result in an onshore bias to these velocities. It is therefore not clear whether the measured velocities are dominated by wind or a mean onshore surface current. However, as the water depth decreases, the effect of any subsurface offshore directed current (undertow) "felt" by the surface waves would increase, thus causing the velocities measured by the radar to be less than those further offshore between $x = 80$ to 100 m.

[33] While these explanations for the observed velocities are plausible, they do not address why the techniques differ from the range-time derived bore celerities or the shallow water model. Although the range-time derived bore celerities are close to the dispersion relationship, they are slightly lower than predicted values. This could be a result of oblique bore propagation. For example, a mean incident wave angle of 7° from shore normal minimizes the RMS difference between the range-time derived bore celerities and the model. It also yields range-time bore celerities that are closer to the Doppler and PIV estimates. Differences between PIV and the model were largest at the offshore locations, likely due to the infrequent occurrence of broken waves and spatial averaging, and decreased in the onshore

direction to a minimum in the inner surf zone where broken waves are prevalent.

[34] In contrast to PIV, Doppler radar bore celerities are systematically larger than expected. Since radar velocities are measured from the Doppler shift of the backscattered electromagnetic wave due to ensemble particle motions, the Doppler velocity includes the radial components of both the alongshore current and cross-shore motion of the bores. Any southward propagating alongshore current will therefore increase the Doppler bore estimates. For a bore propagation angle of $7°$, an alongshore surface current of 0.44 m s^{-1} is required to minimize the RMS difference between the Doppler bore estimates and the range-time derived bore celerities. This current velocity may be too large for the wave conditions during the collection period and thus may not completely explain the difference. Other factors such as the speed of the turbulent water tumbling down the bore face, sea spray and shore-directed water particle ejections resulting from breaking can also contribute to the Doppler velocities.

6. Conclusion

[35] This study has presented surface velocity measurements from the surf and swash zones using two remote sensing instruments. Comparisons of velocities from various cross-shore locations have been used to investigate each technique under different nearshore conditions. The study has also attempted to provide an interpretation of the measured velocities in the context of the imaging mechanisms used by each sensor.

[36] Qualitative image comparisons showed excellent agreement in which regions of high radar backscatter corresponded to bores visible in the video imagery. Direct velocity comparisons between the two techniques at several cross-shore locations yielded r^2 correlation coefficients up to 0.60. Spectral decomposition of the times series were also similar as evidenced by high coherence in the low frequency to incident band (roughly 0.02 to 0.25 s^{-1}) with 95% confidence levels for phase shifts spanning $0°$. Neither technique observed significant offshore-directed motions because of a lack of offshore-directed surface motion or because the sensors are incapable of measuring such motions when they existed. PIV was found to be vulnerable to errors in conditions of insufficient surface texture while the radar appeared susceptible to errors close to shore where, away from the bore, water smoothness may adversely affect the measurement. In addition, both techniques are affected by spatial smoothing.

[37] This comparison has shown that care is needed in interpreting microwave radar and PIV remote sensing measurements of the nearshore region. Specifically, the techniques provided estimates of swash zone velocities and surf zone bore celerities with typical relative errors of 15−25% compared to velocities derived from the slope of the range-time bore front trajectory, which in turn compared well with a shallow water dispersion relationship. The most significant difference in the PIV occurred at the two offshore locations whereas the radar showed a consistent over prediction of the bore celerities with the most significant difference in the swash zone. The bimodal distribution of microwave Doppler radar velocities indicated that the radar

measurements were significantly influenced by the bore celerities during bore propagation inside the surf zone and a superposition of capillary, wind-driven and shore-directed wave velocities in between bores. PIV was found to be capable of estimating bore celerities inside the surf zone, and more closely matched the celerity estimates of a shallow water model. Due to intermittent lack of image texture, PIV was often less sensitive than radar at measuring the surface fluid velocities between bore fronts. However, PIV was able to typically track both uprush and backwash swash zone surface velocities when adequate image texture was present, whereas radar infrequently measured backwash velocities.

[38] Measurements made with remote sensors have the potential to further our understanding of nearshore hydrodynamics and wave motions resulting from the larger spatial coverage and non-interference with the flow field. In addition, remote sensors often reduce logistical deployment difficulties, require low maintenance and can be cost-effective. Results from this study offer insight into the use of two remote sensing techniques in the surf and swash zones, which will be important in the interpretation of measurements from future remote sensing studies.

References

Bell, P. S., Shallow water bathymetry derived from an analysis of X-band marine radar images of waves, *Coastal Eng.*, 37, 513−527, 1999.

Chang, K. A., and P. L.-F. Liu, Velocity, acceleration and vorticity under a breaking wave, *Phys. Fluids*, 10(1), 327−329, 1998.

Chickadel, C., and R. A. Holman, Measuring longshore current with video techniques, *Eos Trans. AGU*, 82(47), Fall Meeting Suppl., OS21C-09, 2001.

Dugan, J. P., H. H. Suzukawa, C. P. Forsyth, and M. S. Farber, Ocean wave dispersion surface measured with airborne IR imaging system, *IEEE Trans. Geosci. Remote Sens.*, 34(5), 1282−1284, 1996.

Dugan, J. P., G. J. Fetzer, J. Bowden, G. J. Farruggia, J. Z. Williams, C. C. Piotrowski, K. Vierra, D. C. Campion, and D. N. Sitter, Airborne optical system for remote sensing of ocean waves, *J. Atmos. Oceanic Technol.*, 18(7), 1267−1276, 2001a.

Dugan, J. P., C. C. Piotrowski, and J. Z. Williams, Water depth and surface current retrievals from airborne optical measurements of surface gravity wave dispersion, *J. Geophys. Res.*, 106(C8), 16,903−16,915, 2001b.

Earnshaw, H. C., T. Bruce, C. A. Greated, and W. J. Easson, PIV measurements of oscillatory flow over a rippled bed, in *Proceedings of the 24th International Conference on Coastal Engineering*, edited by B. L. Edge, Am. Soc. of Civ. Eng., Reston, Va., 1994.

Frasier, S. J., and R. E. McIntosh, Observed wavenumber-frequency properties of microwave backscatter from ocean surface at near-grazing angles, *J. Geophys. Res.*, 101(C8), 18,391−18,407, 1996.

Frasier, S. J., Y. Liu, D. Moller, R. E. McIntosh, and C. Long, Directional ocean wave measurements in a coastal setting using focused array imaging radar, *IEEE Trans. Geosci. Remote Sens.*, 33(2), 428−440, 1995.

Graber, H. C., D. R. Thompson, and R. E. Carande, Ocean surface features and currents measured with synthetic aperture radar interferometry and HF radar, *J. Geophys. Res.*, 101(C11), 25,813−25,832, 1996.

Gray, C., and C. A. Greated, The application of PIV to the study of water waves, *Opt. Lasers Eng.*, 9, 265−276, 1988.

Hart, D. P., High-speed PIV analysis using compressed image correlation, *J. Fluids Eng.*, 120(3), 463−470, 1998.

Holland, K. T., Application of the linear dispersion relation with respect to depth inversion and remotely sensed imagery, *IEEE Trans. Geosci. Remote Sens.*, 39(9), 2060−2072, 2001.

Holland, K. T., and R. A. Holman, Video estimation of foreshore topography using trinocular stereo, *J. Coastal Res.*, 13(1), 81–87, 1997.

Holland, K. T., R. A. Holman, T. C. Lippmann, J. Stanley, and N. Plant, Practical use of video imagery in nearshore oceanographic field studies, *IEEE J. Oceanic Eng.*, 22(1), 81–92, 1997.

Holland, K. T., J. A. Puleo, and T. Kooney, Quantification of swash flows using video-based particle image velocimetry, *Coastal Eng.*, 44, 65–77, 2001.

Holman, R. A., T. C. Lippmann, P. V. O'Neill, and K. Hathaway, Video estimation of subaerial beach profiles, *Mar. Geol.*, 97(1–2), 225–231, 1991.

Holman, R. A., A. H. Sallenger Jr., T. C. Lippmann, and J. W. Haines, The application of video image processing to the study of nearshore processes, *Oceanography*, 6(3), 78–85, 1993.

Lippmann, T. C., and R. A. Holman, Quantification of sand bar morphology: A video technique based on wave dissipation, *J. Geophys. Res.*, 94(C1), 995–1011, 1989.

Lippmann, T. C., and R. A. Holman, The spatial and temporal variability of sand bar morphology, *J. Geophys. Res.*, 95(C7), 11,575–11,590, 1990.

Lippmann, T. C., and R. A. Holman, Phase speed and angle of breaking waves measured with video techniques, in *Coastal Sediments '91*, edited by N. C. Kraus, K. J. Gingerich, and D. L. Kriebel, pp. 542–556, Am. Soc. of Civ. Eng., Reston, Va., 1991.

Marom, M., L. Shemer, and E. B. Thornton, Energy density directional spectra of nearshore wave field measured by interferometric synthetic aperture radar, *J. Geophys. Res.*, 96(C12), 22,125–22,134, 1991.

McGregor, J. A., E. M. Poulter, and M. J. Smith, Ocean surface currents obtained from microwave sea-echo Doppler spectra, *J. Geophys. Res.*, 102(C11), 25,227–25,236, 1997.

McGregor, J. A., E. M. Poulter, and M. J. Smith, S band Doppler radar measurements of bathymetry, wave energy fluxes, and dissipation across an offshore-bar, *J. Geophys. Res.*, 103(C9), 18,779–18,789, 1998.

McIntosh, R. E., S. J. Frasier, and J. B. Mead, FOPAIR: A focused phased array imaging radar for ocean remote sensing, *IEEE Trans. Geosci. Remote Sens.*, 33(1), 115–124, 1995.

Miller, K. S., and M. M. Rochwarger, A covariance approach to spectral moment estimation, *IEEE Trans. Inf. Theory*, 18(5), 588–596, 1972.

Moller, D., S. J. Frasier, D. L. Porter, and R. E. McIntosh, Radar-derived inferometric surface currents and their relationship to subsurface current structure, *J. Geophys. Res.*, 103(C6), 12,839–12,852, 1998.

Plant, W. J., E. A. Terray, R. A. J. Petitt, and W. C. Kellar, The dependence of microwave backscatter from the sea on illuminated area: Correlation times and lengths, *J. Geophys. Res.*, 99(C5), 9705–9723, 1994.

Poulter, E. M., M. J. Smith, and J. A. McGregor, S-band FMCW radar measurements of ocean surface dynamics, *J. Atmos. Oceanic Technol.*, 12(6), 1271–1286, 1995.

Puleo, J. A., and K. T. Holland, Field observations of three-dimensional swash flow patterns and morphodynamics, in *Proceedings of the 27th International Conference on Coastal Engineering*, edited by B. L. Edge, pp. 637–650, Am. Soc. of Civ. Eng., Reston, Va., 2000.

Raubenheimer, B., R. T. Guza, and S. Elgar, Wave transformation across the inner surf zone, *J. Geophys. Res.*, 101(C11), 25,589–25,597, 1996.

Ruessink, B. G., P. S. Bell, I. M. J. van Enckevort, and S. G. J. Aarninkhof, Nearshore bar crest position quantified from time-averaged X-band radar images, *Coastal Eng.*, 45, 19–32, 2002.

Senet, C. M., J. Seemann, and F. Ziemer, The near-surface current velocity determined from image sequences of the sea surface, *IEEE Trans. Geosci. Remote Sens.*, 39(3), 492–505, 2001.

She, K., C. A. Greated, and W. J. Easson, Experimental of 3-dimensional breaking wave kinematics, *Appl. Ocean Res.*, 19(5–6), 329–343, 1997.

Shemer, L., M. Marom, and D. Markman, Estimates of currents in the nearshore ocean region using interferometric synthetic aperture radar, *J. Geophys. Res.*, 98(C4), 7001–7010, 1993.

Stockdon, H. F., and R. A. Holman, Estimation of wave phase speed and nearshore bathymetry from video imagery, *J. Geophys. Res.*, 105(C9), 22,015–22,033, 2000.

Wolf, J., and P. S. Bell, Waves at Holderness from X-band radar, *Coastal Eng.*, 42, 247–263, 2001.

Wright, J. W., A new model for sea clutter, *IEEE Trans. Antenna Propag.*, 16, 217–223, 1968.

Young, I. R., W. Rosenthal, and F. Ziemer, A 3-dimensional analysis of marine radar images for the determination of ocean wave directionality and surface currents, *J. Geophys. Res.*, 90(C1), 1049–1059, 1985.

———————————————

G. Farquharson and S. J. Frasier, Microwave Remote Sensing Laboratory, Knowles Engineering Building, University of Massachusetts, Amherst, MA 01003, USA. (gordon@mirsl.ecs.umass.edu; frasier@ecs.umass.edu)

K. T. Holland and J. A. Puleo, Naval Research Laboratory, Marine Geosciences Division, Code 7440.3 Building 2438, Stennis Space Center, MS 39529, USA. (tholland@nrlssc.navy.mil; jpuleo@nrlssc.navy.mil)